Article

Using non-Fourier's heat flux and non-Fick's mass flux theory in the Radiative and Chemically reactive flow of Powell-Eyring fluid

Hina Firdous [1], Syed Tauseef Saeed [1,*], Hijaz Ahmed [2] and Syed Muhammad Husnine [1]

[1] Department of Sciences and Humanities, National University of Computer and Emerging Sciences, Lahore Pakistan; hina.firdous@nu.edu.pk (H.F); tauseefsaeed301@gmail.com (S.T.S); syed.husnine@nu.edu.pk (S.H)

[2] Section of Mathematics, International Telematic University Uninettuno, Corso Vittorio Emanuele II 39, 00186 Roma, Italy; hijaz555@gmail.com

* Correspondence: tauseefsaeed301@gmail.com (S.T.S); hijaz555@gmail.com (H.A)

Abstract: The behavior of convective boundary conditions is studied to delineate their role in heat and mass relegation in the presence of radiation, chemical reaction, and hydromagnetic forces in three-dimensional Powell-Eyring nanofluids. Implications concerning non-Fourier's heat flux and non-Fick's mass flux with respect to temperature nanoparticle concentration were examined to discuss the graphical attributes of the principal parameters. An efficient optimal homotopy analysis method is used to solve the transformed partial differential equations. Tables and graphs are physically interpreted for significant parameters

Keywords: Eyring-Powell fluid; Non-Fourier's heat flux and non-Fick's mass flux theory; Boundary layer flow; Radiation; Convective boundary conditions.

1. Introduction

Heat transfer is mainly observed due to variation in temperature of bodies. This process has a vital role in mechanization and industry like climate engineering, cooling of devices, nuclear power plants, and energy acquirement. The well-known Fourier law for heat transfer [1] and Fick's law for mass transfer have been widely used in literature. The fragility of Fourier law is that the initial bugging is immediately perceived by the medium, which is unpractical. Classical Fourier law was amended by adding relaxation time to heat flux by Cattaneo [2]. Christov [3] further modified the Cattaneo's law by incorporating a Lie derivative for the heat flux. The Cattaneo-Christov theory has been applied to both Newtonian and non-Newtonian fluids with various physiological effects. The Cattaneo-Christov model was discussed by Straughan for the thermal convection of a viscous fluid [4]. Salahuddin et al. [5] applied theory given in [3] to Williamson fluid. The flow of Eyring-Powell fluid over an exponential stretching surface in three dimensions was reported by Hayat and Nadeem [6] following [3]. With the same theory, the Maxwell fluid flow was studied past an expanding sheet with changeable thickness by Hayat et al. [7]. Moreover, Hashim and Khan [8] considered Carreau fluid with a slender sheet under the effect of model [3]. The Oldroyd-B fluid was analyzed employing [3] by Abbasi et al. [9]. Hayat et al. [10] gave a comparative study of visco-elastic fluids through [3]. Unsteady and nonlinear convection of micro-and nanofluids under [3] is recently stated by Upadhya et al. [11].

Non-Newtonian fluids have extensive use in industrial and engineering processes such as production of paper, polymer processing, geological flows in the earth mantle, ink

printing, paint suspensions, and biological flows. Thus, the analysis of such fluids is of substantial research and significance importance. Powell and Eyring presented an integral mathematical model for a non-Newtonian fluid well known as Eyring-Powell fluid model [12]. The model is dominant to the other nonlinear models as it can depreciate to visco fluids for immense and limited shear rates. Moreover, the model is deduced from the kinetic theory of fluids rather than empirical relations. Considering the importance of this non-Newtonian fluid, Hayat et al. [13] analyzed the steady flow of [12]. The peristaltic flow of Eyring-Powell nanofluid in an endoscope was investigated by Akbar and Nadeem [14]. Boundary layer flow of [12] was examined numerically by Jalil et al. [15]. Malik et al. [16] investigated boundary layer flow in a stretching cylinder with variable viscosity for the fluid characterized by constitutive equations due to Powell and Eyring. Mixed convected flow of [12] along a rotating cone was presented by Nadeem and Saleem [17]. The role of hybrid Eyring-Powell nano fluid [18] is observed for peristaltic transport. Hayat et al. [19] presented results for the axisymmetric radial flow of [12] over an impermeable stretching surface and the heat transfer process was analyzed through convective boundary conditions. Most Recently, Ibrahim [20] proposed the numerical solution for the rotating Eyring Powell fluid flow in three dimensions with theory [3].

Magneto fluid dynamics has become an important topic in recent years. The study of magneto hydrodynamics has won real life applications, for instance, electromagnetic forces can be used to pump liquid metals without the need for any moving parts. MHD has significant importance in stellar and planetary processes as well. The concept of MHD has also boosted the engineering applications. For example, the direct conversion generator and flow problems of ionized gasses. The MHD unsteady flow in a porous channel with convective heat conditions at the surface has been explored by Makinde [21] and the study concludes that the presence of magnetic field strengthens the flow control. The boundary layer flow of MHD Maxwell nanofluid was discussed with numerical aid [22]. Ellahi et al. [23] numerically inquired the Coutte flow of [12] and heat transfer in magnetohydrodynamics. Thermal radiation is a ruling factor in the thermo dynamic analysis of high temperature systems like boilers and solar connectors. The heat and mass relocation analysis with thermal radiation play a vital role in manufacturing industries. For instance, the design of flippers, gas motors, cooling towers and various propulsion devices for aircraft, energy utilization, food processing as well as diverse agricultural, military, and health applications. As a result, much work has been done on fluid flow considering radiation in thermal radiation. Analysis has been carried out for viscoelastic fluid in the effect of thermal radiation and the Rosseland approximation is applied to characterize the heat flux in the heat equation by Qasim et al. [24]. Ayub et al. [25] discuss holdings of wall shield on the radiation of the transverse electromagnetic wave. The solution is obtained by the Wiener–Hopf technique. A short time ago, Raju et al. [26] address the buoyancy accommodating heat and mass transfer considering thermal radiation and Buongiorno's model. The results were presented for the flow behavior over a paraboloid, a cone, and a cylinder adopting numerical method.

 doi:10.20944/preprints202109.0157.v1

Many of the modern propositions in technology are intended on making small devices. This can improve the efficiency scale and enhance the productivity. Similarly, advances are also occurring in fluid dynamics at a rapid pace known as micro fluidics and nanofluidics. The application includes the designing of electronic gadgets, polyphase flows in lab-on-a-chip, and basic procedures in individual biological cells. Due to the enormous applications of nanofluids, many researchers have shown their interest in the studing effects of nanoparticles in non-Newtonian fluids on different physiological aspects [27–32].

Above literature motivated us to target the analytical solutions of three-dimensional rotating Eyring Powell fluid inclusive of magnetohydrodynamics, radiation effects, and convective boundary conditions with [3]. Convergent series solutions by the optimal homotopy approach are constructed [33–37]. The impact of important parameters on velocity components, temperature, and concentration are illustrated graphically. However, skin friction, Nusselt number, and Sherwood numbers are tabulated numerically.

2. Mathematical Formulation

The mathematical design of the non-Newtonian fluid called Powell-Eyring fluid is investigated. For this purpose, the stress tensor of the fluid is taken from [12].

$$D = -PI + \mu W + \frac{1}{\beta\dot{\xi}}\sinh\left(\frac{1}{d}\dot{\xi}\right)W, \tag{1}$$

Here μ is the dynamic viscosity, β *and* d are the rheological Powell-Eyring fluid model parameters. $\dot{\xi} = \sqrt{\frac{1}{2}trW^2}$ and $W = \nabla V + (\nabla V)^T$ so that the second-order approximation of $\sinh^{-1}$ after using Taylor series expansion is

$$sinh^{-1}\left(\frac{1}{d}\dot{\xi}\right) \approx \left(\frac{1}{d}\dot{\xi}\right) - \frac{1}{6}\left(\frac{1}{d}\dot{\xi}\right)^3, \qquad \left|\frac{1}{2}\dot{\xi}\right| \ll 1 \tag{2}$$

Hence Eq. (1) takes the form

$$D = PI + \left(\mu + \frac{1}{\beta d}\right)W - \frac{1}{6\beta d^3}\left(\dot{\xi}\right)^3 W.$$

The chemical reaction effect of MHD steady and incompressible Powell-Eyring nano fluid in the presence of thermal radiation over two-sided stretching sheet with [3] is explored. The coordinate system fixed in the xy-plane such that the extending velocities at the layer in both x and y directions are $u = ax, v = by$, where $a > 0$ and $b > 0$ are constants. Magnetic field B is applied perpendicular to the flow direction, as the fluid is flowing in the space $z \geq 0$. Furthermore, the fluid is rotating with uniform angular velocity υ about z-axis. The sheet temperature is constant and assumed to be greater than the outside temperature $T_w > T_\infty$. C_w is the nanoparticles concentration at the surface and C_∞ is given as the ambient concentration. Under these assumptions, the boundary layer flow is driven by the following conservation laws of mass, momentum, and energy.

 doi:10.20944/preprints202109.0157.v1

$$\frac{\partial u}{\partial x}+\frac{\partial v}{\partial y}+\frac{\partial w}{\partial z}=0, \tag{3}$$

$$u\frac{\partial u}{\partial x}+v\frac{\partial u}{\partial y}+w\frac{\partial u}{\partial z}-2\mathfrak{V}v=\left(\upsilon+\frac{1}{\rho\beta d}\right)\left(\frac{\partial^2 u}{\partial z^2}\right)-\frac{1}{2\rho\beta d^3}\left(\frac{\partial u}{\partial z}\right)^2\frac{\partial^2 u}{\partial z^2}-\frac{\sigma B^2}{\rho}u, \tag{4}$$

$$u\frac{\partial v}{\partial x}+v\frac{\partial v}{\partial y}+w\frac{\partial v}{\partial z}+2\mathfrak{V}u=\left(\upsilon+\frac{1}{\rho\beta d}\right)\left(\frac{\partial^2 v}{\partial z^2}\right)-\frac{1}{2\rho\beta d^3}\left(\frac{\partial v}{\partial z}\right)^2\frac{\partial^2 v}{\partial z^2}-\frac{\sigma B^2}{\rho}v, \tag{5}$$

$$u\frac{\partial T}{\partial x}+v\frac{\partial T}{\partial y}+w\frac{\partial T}{\partial z}=\alpha_t\left(\frac{\partial^2 T}{\partial z^2}\right)-\nabla\cdot\chi_q-\frac{1}{\rho c_p}\frac{\partial q_r}{\partial z}+\Lambda\left\{D_B\left(\frac{\partial C}{\partial z}\frac{\partial T}{\partial z}\right)+\frac{D_T}{T_\infty}\left(\frac{\partial T}{\partial z}\right)^2\right\}, \tag{6}$$

$$u\frac{\partial C}{\partial x}+v\frac{\partial C}{\partial y}+w\frac{\partial C}{\partial z}=D_B\left(\frac{\partial^2 C}{\partial z^2}\right)+\frac{D_T}{T_\infty}\left(\frac{\partial^2 T}{\partial z^2}\right)-Q(C-C_\infty), \tag{7}$$

Cattaneo-Christov theory is incorporated inplace of classical Fourier's heat flux law and Fick's mass flux law of diffusion [3]. The equations involving heat flux χ_q and mass flux χ_J are given.

$$\chi_q+\lambda_q\left(\frac{\partial\chi_q}{\partial t}+V.\nabla\chi_q-\chi_q.\nabla V+(\nabla.V)\chi_q\right)=-K\nabla T \tag{8}$$

$$\chi_J+\lambda_J\left(\frac{\partial\chi_J}{\partial t}+V.\nabla\chi_J-\chi_J.\nabla V+(\nabla.V)\chi_J\right)=-D_B\nabla C \tag{9}$$

where λ_q is the thermal relaxation time and λ_J is the concentration relaxation time. To proceed further, we use the Rosseland approximation for the radiative heat flux q_r.

$$q_r=-\frac{4\sigma_s}{3K_e}\frac{\partial T^4}{\partial z}. \tag{10}$$

Expanding T^4 into Taylor series about T_∞ and neglecting higher order terms

$$T^4=4T_\infty^3T-3T_\infty^4. \tag{11}$$

In accordance with the above supposition, the heat and mass transfer equation will reduce to

$$u\frac{\partial T}{\partial x}+v\frac{\partial T}{\partial y}+w\frac{\partial T}{\partial z}=-\lambda_q\left[\begin{array}{l}u^2\frac{\partial^2 T}{\partial x^2}+v^2\frac{\partial^2 T}{\partial y^2}+w^2\frac{\partial^2 T}{\partial z^2}+2uv\frac{\partial^2 T}{\partial x\partial y}+2vw\frac{\partial^2 T}{\partial y\partial z}+2uw\frac{\partial^2 T}{\partial x\partial z}+\\ \left(u\frac{\partial u}{\partial x}+v\frac{\partial u}{\partial y}+w\frac{\partial u}{\partial z}\right)\frac{\partial T}{\partial x}+\left(u\frac{\partial v}{\partial x}+v\frac{\partial v}{\partial y}+w\frac{\partial v}{\partial z}\right)\frac{\partial T}{\partial y}+\left(u\frac{\partial w}{\partial x}+v\frac{\partial w}{\partial y}+w\frac{\partial w}{\partial z}\right)\frac{\partial T}{\partial z}\end{array}\right]$$
$$+\alpha_t\frac{\partial^2 T}{\partial z^2}-\frac{16\sigma_s T_\infty^3}{3K_e\rho c_p}\frac{\partial^2 T}{\partial z^2}+\Lambda\left[D_B\left(\frac{\partial C}{\partial z}\frac{\partial T}{\partial z}\right)+\frac{D_T}{T_\infty}\left(\frac{\partial T}{\partial z}\right)^2\right], \tag{12}$$

Preprints (www.preprints.org) | NOT PEER-REVIEWED | Posted: 8 September 2021 doi:10.20944/preprints202109.0157.v1

$$u\frac{\partial C}{\partial x}+v\frac{\partial C}{\partial y}+w\frac{\partial C}{\partial z}=-\lambda_J\left[\begin{array}{l}u^2\frac{\partial^2 C}{\partial x^2}+v^2\frac{\partial^2 C}{\partial y^2}+w^2\frac{\partial^2 C}{\partial z^2}+2uv\frac{\partial^2 C}{\partial x\partial y}+2vw\frac{\partial^2 C}{\partial y\partial z}+2uw\frac{\partial^2 C}{\partial x\partial z}+\\ \left(u\frac{\partial u}{\partial x}+v\frac{\partial u}{\partial y}+w\frac{\partial u}{\partial z}\right)\frac{\partial C}{\partial x}+\left(u\frac{\partial v}{\partial x}+v\frac{\partial v}{\partial y}+w\frac{\partial v}{\partial z}\right)\frac{\partial C}{\partial y}+\left(u\frac{\partial w}{\partial x}+v\frac{\partial w}{\partial y}+w\frac{\partial w}{\partial z}\right)\frac{\partial C}{\partial z}\end{array}\right]$$

$$+D_B\frac{\partial^2 C}{\partial z^2}+\frac{D_T}{T_\infty}\left(\frac{\partial^2 T}{\partial z^2}\right)-Q(C-C_\infty). \tag{13}$$

where σ_s is the Stefan-Boltzmann constant and K_e is the mean absorption coefficient. The boundary conditions associated with the study are

$$\begin{aligned}&u=u(x)=ax,\ \ v=v(y)=by,\ \ w=0,\\ &-K\frac{\partial T}{\partial z}=H_1(T_w-T),\ \ -D_B\frac{\partial C}{\partial z}=H_2(C_w-C)\ at\ z=0\\ &u\to 0,\ \ v\to 0,\ \ T\to T_\infty,\ \ C\to C_\infty\quad as\ z\to\infty.\end{aligned} \tag{14}$$

Selecting the following similarity transformations

$$\begin{aligned}&\eta=\sqrt{\frac{a}{\upsilon}}z,\ \ u=axf'(\eta),\ \ v=ayg'(\eta),\ \ w=-\sqrt{a\upsilon}\left(f(\eta)+g(\eta)\right),\\ &\theta(\eta)=\frac{T-T_\infty}{T_w-T_\infty},\ \ \varphi(\eta)=\frac{C-C_\infty}{C_w-C_\infty}.\end{aligned} \tag{15}$$

The continuity equation is satisfied and the rest of nondimensional governing equations are

$$(1+n)f'''-ne_1(f'')^2f'''-f'^2+(f+g)f''+2\gamma\Omega g'-Mf'=0, \tag{16}$$

$$(1+n)g'''-ne_2(g'')^2g'''-g'^2+(f+g)g''-2\frac{\Omega}{\gamma}f'-Mg'=0, \tag{17}$$

$$\left(1+\tfrac{4}{3}N_1\right)\theta''+P_r\left(N_b\varphi'\theta'+N_t\theta'^2+(f+g)\theta'-\delta_t(f+g)(f'+g')\theta'+(f+g)^2\theta''\right)=0, \tag{18}$$

$$\varphi''+\left(N_t/N_b\right)\theta''+S_c\left((f+g)\varphi'-\delta_c(f+g)(f'+g')\varphi'+(f+g)^2\varphi''-\varepsilon\varphi\right)=0. \tag{19}$$

The corresponding boundary conditions are

$$\begin{aligned}&f(0)=g(0)=0,\ \ f'(0)=1,\ \ g'(0)=A,\\ &\theta'(0)=-\alpha_1\left(1-\theta(0)\right),\ \ \varphi'(0)=-\alpha_2\left(1-\varphi(0)\right)\ \ at\ \eta=0.\\ &f'(\infty)\to 0,\ \ g'(\infty)\to 0,\ \ \theta(\infty)\to 0,\ \ \varphi(\infty)\to 0\quad as\ \eta\to\infty.\end{aligned} \tag{20}$$

Here $n=\frac{1}{\mu\beta d}, e_1=\frac{a^3x^2}{2\upsilon d^2}, e_2=\frac{b^3y^2}{2\upsilon d^2}$ are Eyring-Powell fluid parameters. $A=\frac{b}{a}$ is the stretching ratio parameter. $\Omega=\frac{\upsilon}{a}$ is the rotation parameter and $\gamma=\frac{y}{x}$. $M^2=\frac{\sigma B^2}{a\rho}$ is the

 doi:10.20944/preprints202109.0157.v1

magnetic parameter. $\epsilon = \frac{Q}{a}$ is chemical reaction parameter. $\delta_t = a\lambda_E$, $\delta_c = a\lambda_C$ denotes the nondimensional thermal and concentration relaxation parameter. $N_1 = \frac{4\sigma_s T_\infty^3}{\alpha_t K_e \rho c_p}$ represent thermal radiation parameter. $P_r = \frac{\upsilon}{\alpha_t}$ is Prandtl number. $N_b = {\Lambda D_B (C_w - C_\infty)}/{\upsilon}$ is Brownian motion parameter, $N_t = {\Lambda D_T (T_w - T_\infty)}/{\upsilon T_\infty}$ is thermophoresis parameter. $\alpha_1 = \frac{H_1}{K}\sqrt{\frac{\upsilon}{a}}$ and $\alpha_2 = \frac{H_2}{D_B}\sqrt{\frac{\upsilon}{a}}$ are the heat transfer Biot number and mass transfer Biot number. The engineering components of skin friction coefficient C_f, local Nusselt number Nu_x and the local Sherwood number Sh_x are represented as follows:

$$C_{f_x} = \frac{\tau_{w_x}}{\rho u_{w_x}^2}, \quad C_{f_Y} = \frac{\tau_{w_y}}{\rho v_{w_y}^2}, \quad Nu_x = \frac{x q_w}{K(T_w - T_\infty)}, \quad Sh_x = \frac{x h_w}{D_B (C_w - C_\infty)}, \tag{21}$$

where q_w surface heat flux, h_w surface mass flux, wall shear stress along x-axis τ_{w_x} and wall shear stress along y-axis τ_{w_y} are given by

$$\begin{aligned}
\tau_{w_x} &= \left[\mu\left(\frac{\partial u}{\partial z}\right) + \frac{1}{\beta d}\left(\frac{\partial u}{\partial z}\right) - \frac{1}{6\beta d^3}\left(\frac{\partial u}{\partial z}\right)^3 \right]_{z=0}, \\
\tau_{w_y} &= \left[\mu\left(\frac{\partial v}{\partial z}\right) + \frac{1}{\beta d}\left(\frac{\partial v}{\partial z}\right) - \frac{1}{6\beta d^3}\left(\frac{\partial v}{\partial z}\right)^3 \right]_{z=0}, \\
h_w &= -D_B\left(\frac{\partial C}{\partial z}\right)_{z=0}, \quad q_w = -K\left(\frac{\partial C}{\partial z}\right)_{z=0}
\end{aligned} \tag{22}$$

By incorporating the above equations, we get

$$\begin{aligned}
C_{f_x}\sqrt{R_{e_x}} &= (1+n) f''(0) - \frac{1}{3} n e_1 f''^3(0), \\
C_{f_y}\sqrt{R_{e_y}} &= (1+n) g''(0) - \frac{1}{3} n e_2 g''^3(0), \\
\frac{Nu_x}{\sqrt{R_{e_x}}} &= -\theta'(0), \quad \frac{Sh_x}{\sqrt{R_{e_x}}} = -\varphi'(0).
\end{aligned} \tag{23}$$

Re_x, Re_y are local Reynolds numbers.

3. **Method of solution**

Optimal homotopy method [33-37] is adapted to obtain the solutions for the nonlinear Eqs. (16) to (19) together with boundary conditions. The initial guesses are given as

$$f_0 = 1 - e^{-\eta}, \; g_0 = A(1 - e^{-\eta}), \; \theta_0 = \left(\frac{\alpha_1}{1+\alpha_1}\right) e^{-\eta}, \; \varphi_0 = \left(\frac{\alpha_2}{1+\alpha_2}\right) e^{-\eta}. \tag{24}$$

Preprints (www.preprints.org) | NOT PEER-REVIEWED | Posted: 8 September 2021 doi:10.20944/preprints202109.0157.v1

$$\psi_f(\eta) = f''' - f',\ \psi_g(\eta) = g''' - g',\ \psi_\theta(\eta) = \theta''' - \theta',\ \psi_\varphi(\eta) = \varphi''' - \varphi'. \quad (25)$$

The concept of minimizing the average square residual errors is utilized [33] to find the ideal values of nonzero auxiliary parameters h_0^f, h_0^g, h_0^θ and h_0^φ which are actually responsible for defining the convergence region of homotopy series solutions.

$$E_m^f = \frac{1}{k+1}\sum_{j=0}^{k}\left\{N_f\left(\sum_{i=0}^{m}\hat{f}(\eta),\ \sum_{i=0}^{m}\hat{g}(\eta),\ \sum_{i=0}^{m}\hat{\theta}(\eta),\ \sum_{i=0}^{m}\hat{\varphi}(\eta)\right)_{\eta=j\delta\eta}\right\}^2 d\eta, \quad (26)$$

$$E_m^g = \frac{1}{k+1}\sum_{j=0}^{k}\left\{N_g\left(\sum_{i=0}^{m}\hat{f}(\eta),\ \sum_{i=0}^{m}\hat{g}(\eta),\ \sum_{i=0}^{m}\hat{\theta}(\eta),\ \sum_{i=0}^{m}\hat{\varphi}(\eta)\right)_{\eta=j\delta\eta}\right\}^2 d\eta, \quad (27)$$

$$E_m^\theta = \frac{1}{k+1}\sum_{j=0}^{k}\left\{N_\theta\left(\sum_{i=0}^{m}\hat{f}(\eta),\ \sum_{i=0}^{m}\hat{\theta}(\eta),\ \sum_{i=0}^{m}\hat{\varphi}(\eta)\right)_{\eta=j\delta\eta}\right\}^2 d\eta. \quad (28)$$

$$E_m^\varphi = \frac{1}{k+1}\sum_{j=0}^{k}\left\{N_\varphi\left(\sum_{i=0}^{m}\hat{f}(\eta),\ \sum_{i=0}^{m}\hat{\theta}(\eta),\ \sum_{i=0}^{m}\hat{\varphi}(\eta)\right)_{\eta=j\delta\eta}\right\}^2 d\eta. \quad (29)$$

$$E_m^t = E_m^f + E_m^g + E_m^\theta + E_m^\varphi \quad (30)$$

where E_m^t is the total of the square of residual error, $\boldsymbol{\delta\eta} = 0.5,\ k = 20$.

Mathematica package BVPh2.0 has been used to reduce the average residual error. Table 1 is aligned to show the minimized values of the total residual error at various iterations. In Table 2, the residual errors for f, g, θ, φ are given at three distinct iterations with the 8th-order optimal convergence control parameters. It is evident that the residual errors are reduced by raising iterations. Therefore, OHAM provides a procedure to select any set of local convergence control parameters to find convergent outcomes.

Table 1. Optimal convergence control parameter values and total averaged squared residual errors

Order m	h_0^f	h_0^g	h_0^θ	h_0^φ	E_m^t	CPU time(sec)
2	-0.58	-0.87	-1.90	-1.87	1.89×10^{-4}	14.47
4	-0.53	-1.01	-1.85	-1.84	2.73×10^{-5}	312.73
6	-0.47	-1.08	-1.85	-1.83	1.10×10^{-5}	4452.7
8	-0.43	-1.12	-1.85	-1.84	6.63×10^{-6}	33756.6

Table 2. Individual averaged squared residual errors with optimized values at m = 8 from Table 1

Order m	E_m^f	E_m^g	E_m^θ	E_m^φ	CPU time(sec)
4	1.21×10^{-5}	1.67×10^{-5}	7.46×10^{-6}	6.13×10^{-6}	171.38
8	8.23×10^{-8}	4.53×10^{-7}	3.77×10^{-6}	2.32×10^{-6}	314.38
12	3.91×10^{-9}	4.10×10^{-8}	2.32×10^{-6}	1.07×10^{-8}	506.22

 doi:10.20944/preprints202109.0157.v1

Effect of parameters on Eyring Powell fluid flow

The plots of velocities along x and y direction with coordinate η are executed for the important parameters involved in the flow.

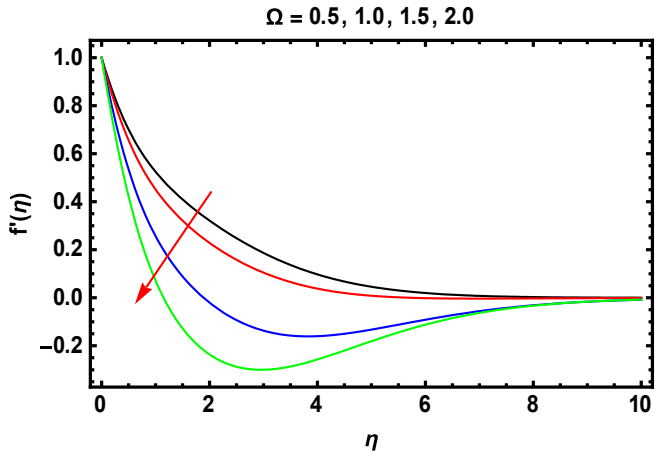

Figure 1. Influence of rotation parameter Ω on the velocity along x-direction.

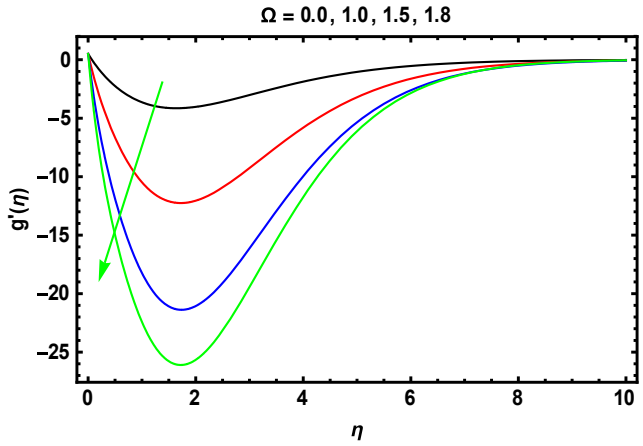

Figure 2. Influence of rotation parameter Ω on the velocity along y-direction.

Preprints (www.preprints.org) | NOT PEER-REVIEWED | Posted: 8 September 2021 doi:10.20944/preprints202109.0157.v1

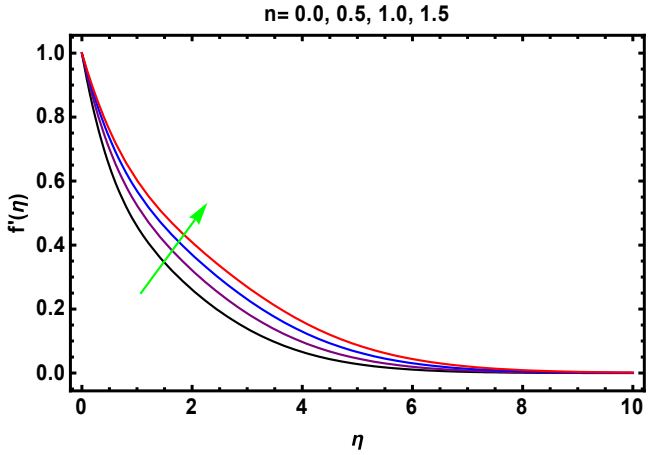

Figure 3. Influence of Eyring-Powell fluid parameter (n) on velocity along x-direction.

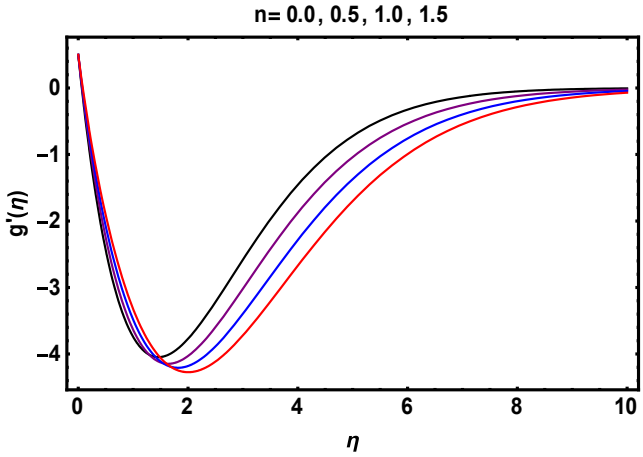

Figure 4. Influence of Eyring-Powell fluid parameter (n) on velocity along y-direction.

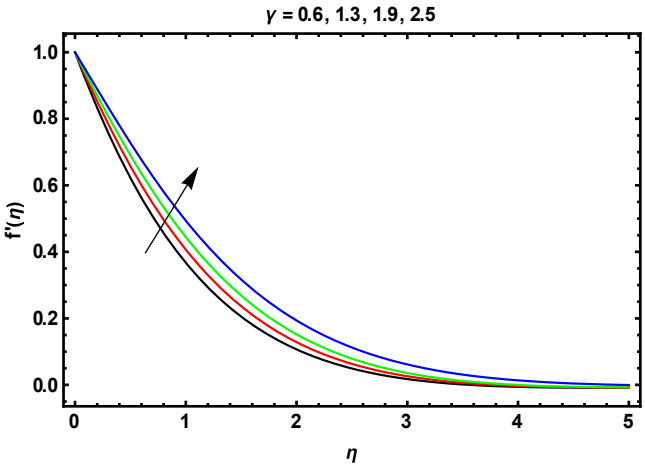

Figure 5. Velocity profile along x-direction for different values of γ

Preprints (www.preprints.org) | NOT PEER-REVIEWED | Posted: 8 September 2021 doi:10.20944/preprints202109.0157.v1

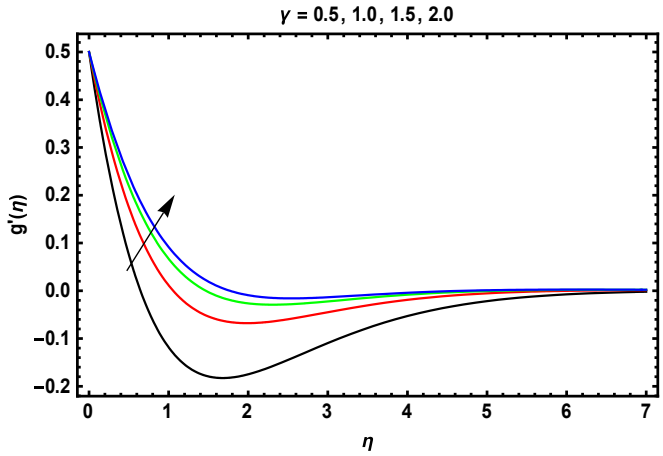

Figure 6. Velocity profile along y-direction for different values of γ.

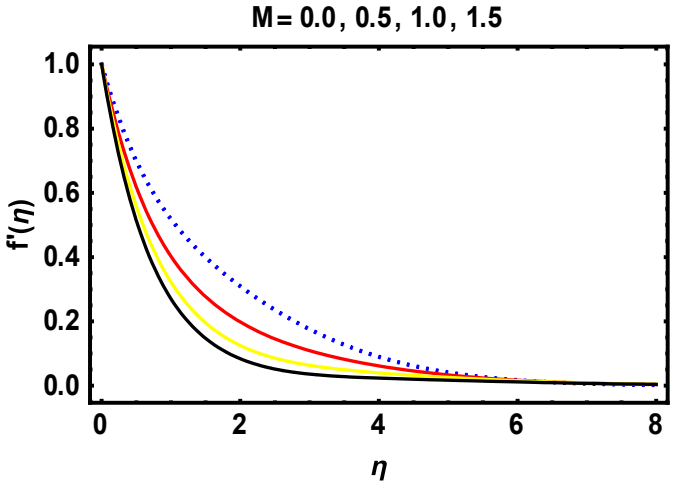

Figure 7. Velocity profile along x-direction for different values of M.

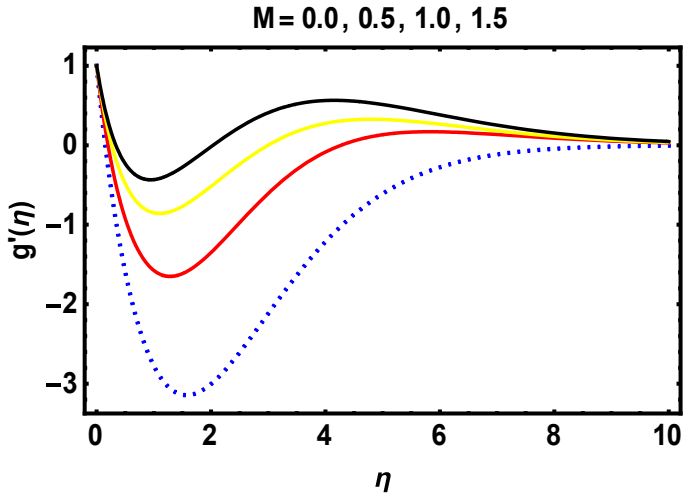

Figure 8. Velocity profile along y-direction for different values of M

Preprints (www.preprints.org) | NOT PEER-REVIEWED | Posted: 8 September 2021 doi:10.20944/preprints202109.0157.v1

Table 3a. Values for $C_{f_x}\sqrt{Re_x}$, when $e_2 = 0.1, \gamma = 0.1, \delta = 0.2, \alpha_1, \alpha_2 = 0.1, M = 0.1, \Omega = 0.5,\ P_r = 0.7, S_c = 0.2$

n / e_1	0.1	0.2	0.3	0.4	0.5
0	0.3790	-0.2230	-1.0345	-2.0887	-3.4222
0.1	0.4052	-0.1505	-0.8864	-1.8077	-2.8865
0.2	0.4309	-0.0803	-0.7474	-1.5610	-2.4658
0.3	0.4561	-0.0123	-0.6158	-1.3391	-2.1205
0.4	0.4807	0.0533	-0.4907	-1.1355	-1.8237
0.5	0.5048	0.1168	-0.3714	-0.9456	-1.5578

Table 3b. Values for $C_{f_x}\sqrt{Re_x}$, when $e_2 = 0.1, \gamma = 0.1, \delta = 0.2, \alpha_1, \alpha_2 = 0.1, M = 0, N_1 = 0, \Omega = 0.5, P_r = 0.7, S_c = 0.2$

n / e_1	0.1	0.2	0.3	0.4	0.5
0	-0.2609	-0.9519	-1.8591	-3.0163	-4.4604
0.1	-0.2304	-0.8671	-1.6750	-2.6393	-3.7018
0.2	-0.2004	-0.7862	-1.5090	-2.3293	-3.1479
0.3	-0.1709	-0.7086	-1.3572	-2.0674	-2.7315
0.4	-0.1419	-0.6339	-1.2168	-1.8405	-2.4049
0.5	-0.1134	-0.5620	-1.0854	-1.6381	-2.1353

Table 4a. Values for $C_{f_y}\sqrt{Re_y}$, when $e_1 = 0.1, \gamma = 0.1, \delta = 0.2, \alpha_1, \alpha_2 = 0.1, M = 0.1, \Omega = 0.5$, $P_r = 0.7, S_c = 0.2$

n / e_2	0.1	0.2	0.3	0.4	0.5
0	55.0297	62.856	71.3146	80.4476	90.2985
0.1	-360.339	-886.582	-1558.52	-2409.23	-3478.23
0.2	-771.59	-1818.44	-3146.07	-4818.55	-6912.48
0.3	-1178.74	-2732.87	-4691.9	-7148.79	-10214.9
0.4	-1581.82	-3630.03	-6196.52	-9401.23	-13388.0
0.5	-1980.84	-4510.1	-7660.48	-11577.1	-16434.2

Preprints (www.preprints.org) | NOT PEER-REVIEWED | Posted: 8 September 2021 doi:10.20944/preprints202109.0157.v1

Table 4b. Values for $C_{f_y}\sqrt{Re_y}$, when $e_1 = 0.1, \gamma = 0.1, \delta = 0.2, \alpha_1, \alpha_2 = 0.1, M = 0, N_1 = 0, \Omega = 0.5,$ $P_r = 0.7, S_c = 0.2$

n / e_2	0.1	0.2	0.3	0.4	0.5
0	52.6231	60.1821	68.3641	77.211	86.766
0.1	-310.516	-772.798	-1366.53	-2122.21	-3076.35
0.2	-669.87	-1589.57	-2762.36	-4247.19	-6114.77
0.3	-1025.46	-2390.28	-4119.65	-6298.98	-9030.92
0.4	-1377.29	-3175.1	-5438.91	-8278.8	-11827.2
0.5	-1725.4	-3944.16	-6720.67	-10187.9	-14506.0

Figure 1 and Figure 2 depict the decrease in velocity along both directions as the rotation in the flow increases. Velocity along y-direction is diminuting more compared to x-direction, this may be because of the retarding force which has more impact along y-direction. Figures 3, 4 narrates the behavior of Powell-Eyring fluid parameter n on the velocities. Velocity ascends by increasing non-Newtonian factors along x-direction, while along y-axis it increases near the surface and descends away from surface. Dimensionless velocities along x and y increase with the increasing ratio γ, as directed in Figures 5, 6. One of the most prime parameters to entertain for flow behavior is the magnetic parameter M. Velocity parallel to y-axis escalates by raising magnetic effects, but the reverse behavior is observed when parallel to x-axis as bent upon by Figures 7, 8. In Table 3a, the skin friction coefficient on the surface is approximated for various values of n and e_1. We observed that the local skin friction coefficient along x-axis is reduced for sufficiently large values of n, hence the smooth flow along x-direction and reverse is the behavior of skin friction co-efficient if e_1 is raised. Skin friction coefficient along y-direction abates for leading values of e_2. In addition, the skin friction co-efficient exceeds for greater values of n $(e_2 \leq 0)$ and recedes for greater values of n $(e_2 > 0)$ as indicated in Table 4a. Tables 3b and 4b are given to analyze the special behavior of local skin friction coefficients in the absence of MHD, radiation and chemical reaction.

 doi:10.20944/preprints202109.0157.v1

Effects of parameters on temperature and concentration

The plots for temperature with coordinate η are executed for the important parameters involved in the heat/ mass transfer.

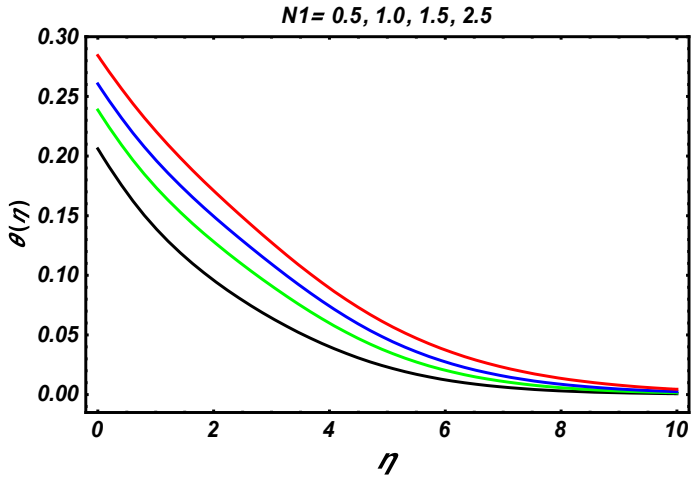

Figure 9. Behavior of radiation parameter N_1 on temperature profile.

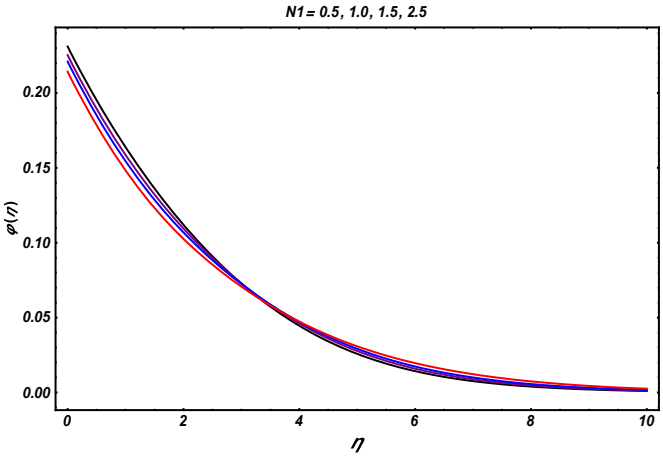

Figure 10. Behavior of radiation parameter N_1 on mass concentration profile.

Preprints (www.preprints.org) | NOT PEER-REVIEWED | Posted: 8 September 2021 doi:10.20944/preprints202109.0157.v1

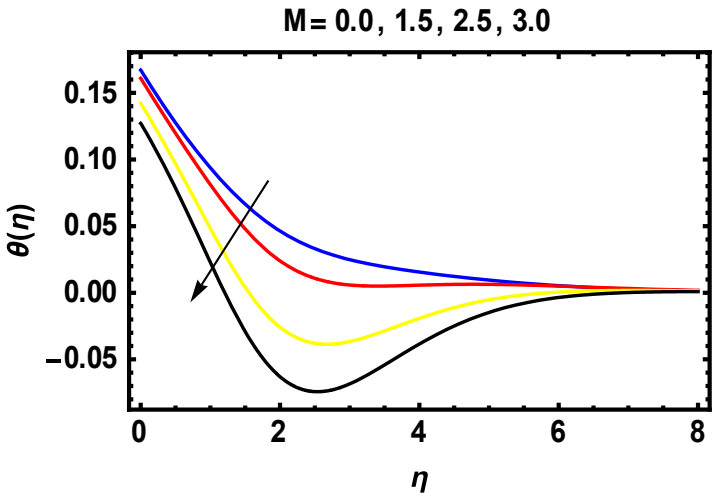

Figure 11. Temperature profile for magnetic parameter M.

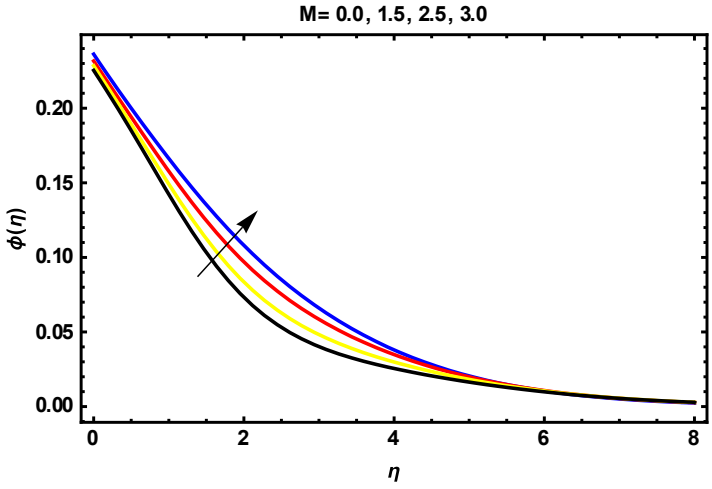

Figure 12. Mass concentration profile for magnetic parameter M.

Preprints (www.preprints.org) | NOT PEER-REVIEWED | Posted: 8 September 2021 doi:10.20944/preprints202109.0157.v1

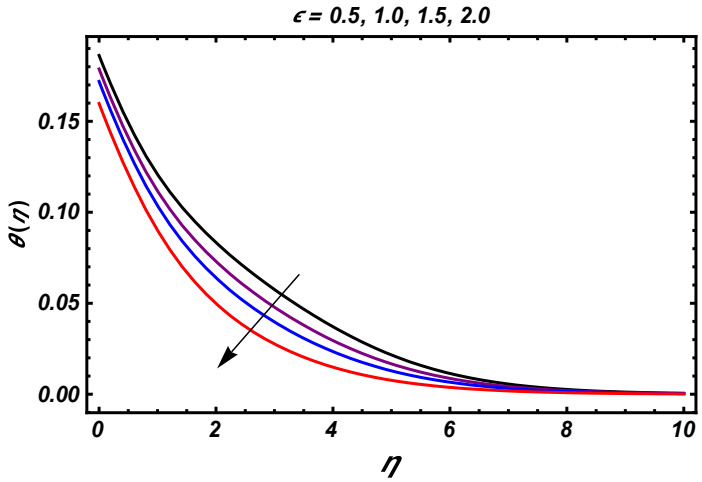

Figure 13. Influence of chemical reaction ϵ on temperature profile.

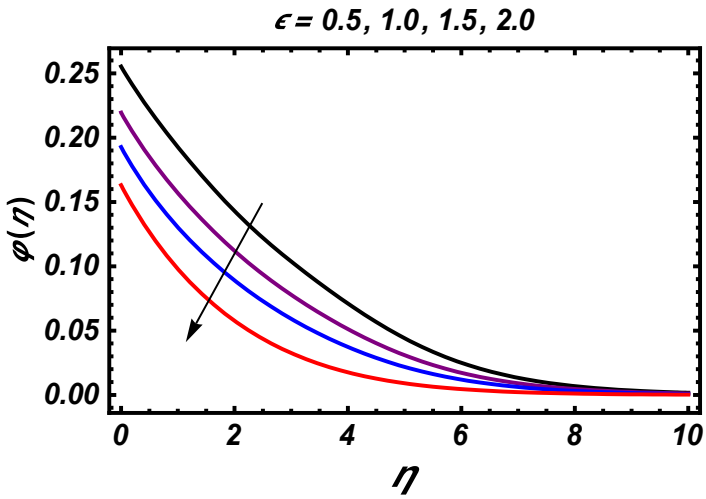

Figure 14. Influence of chemical reaction ϵ on concentration profile.

Preprints (www.preprints.org) | NOT PEER-REVIEWED | Posted: 8 September 2021 doi:10.20944/preprints202109.0157.v1

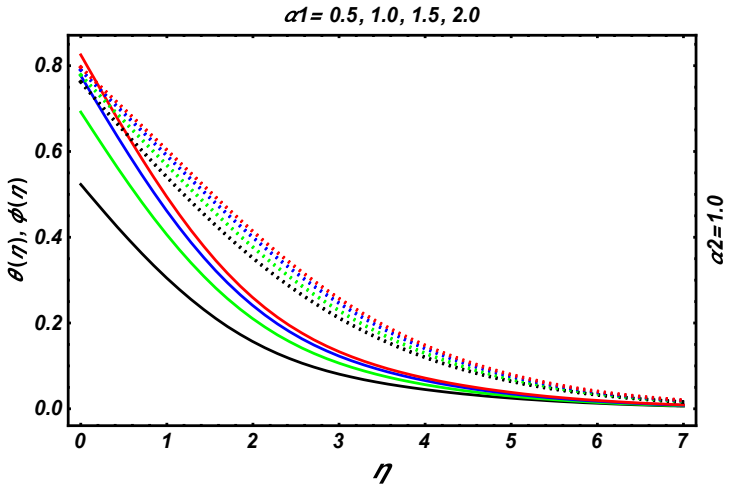

Figure 15.Temperature and concentration graph for different values of α_1.

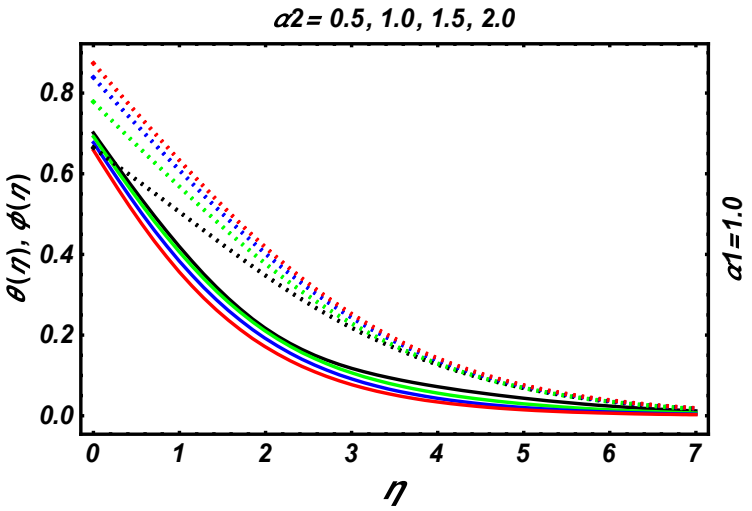

Figure 16. Temperature and concentration graph for different values of α_2.

Preprints (www.preprints.org) | NOT PEER-REVIEWED | Posted: 8 September 2021 doi:10.20944/preprints202109.0157.v1

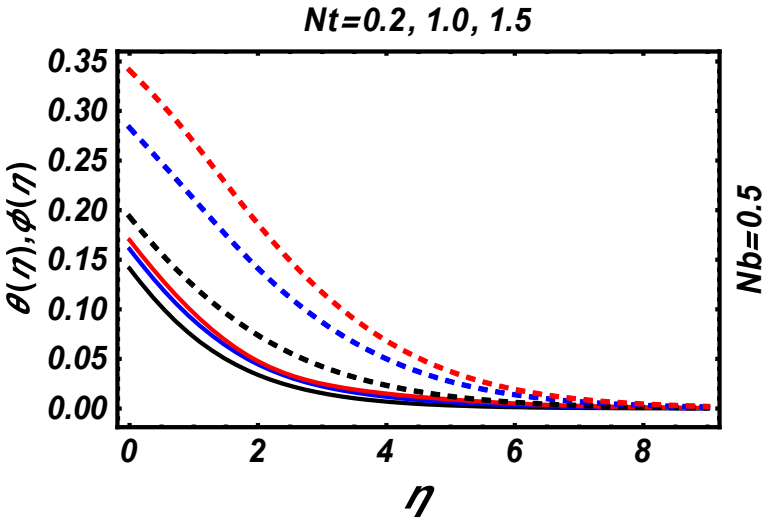

Figure 17. Effect of N_t on temperature and concentration profiles.

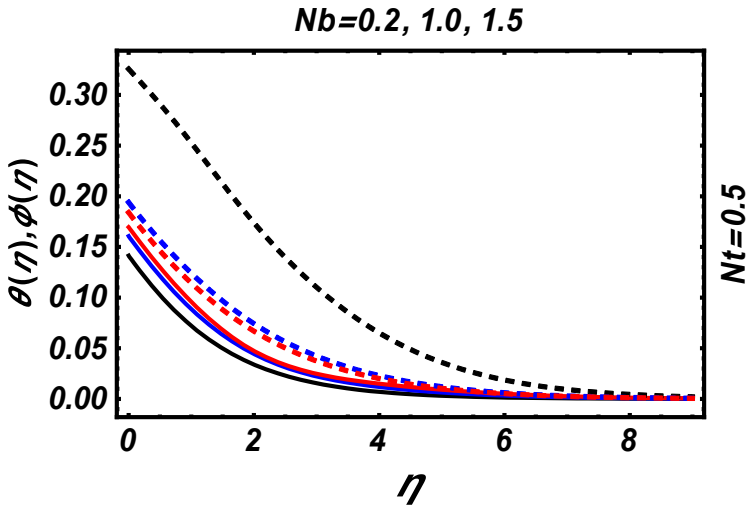

Figure 18. Effect of N_b on temperature and concentration profiles.

Preprints (www.preprints.org) | NOT PEER-REVIEWED | Posted: 8 September 2021 doi:10.20944/preprints202109.0157.v1

Table 5: Computed values of Nusselt no and Sherwood no for different values of $M, N_1, \epsilon, \alpha_1, \alpha_2$

M	N_1	ϵ	α_1	α_2	$-\theta'(0)$	$-\varphi'(0)$
0.1	0.1	0	0.1	0.1		**0.239077**
		0.5				**0.249323**
		1.0				**0.260205**
		1.5				**0.271679**
		2.0				**0.283674**
0		0.1			**0.137712**	**0.14419**
0.5					**0.144231**	**0.145819**
1.0					**0.151694**	**0.147705**
1.5					**0.160144**	**0.149863**
2.0					**0.169628**	**0.152304**
0.1			0	0.5	**0**	**0.722521**
				1.0	**0**	**1.44597**
				2.0	**0**	**2.48147**
			1.0	0.5	**2.46406**	**1.59123**
				1.0	**2.52921**	**2.86485**
				2.0	**2.60205**	**4.53856**
			2.0	0.5	**4.62906**	**2.03578**
				1.0	**4.77689**	**3.58565**
				2.0	**4.94091**	**5.5765**
	0		0.1	0.1	**0.365409**	**0.234357**
	0.5				**0.427331**	**0.277738**
	1.0				**0.58768**	**0.354092**
	1.5				**0.945752**	**0.481151**
	2.0				**1.66287**	**0.68243**

Figure 9 is plotted to analyze the effect of thermal radiation parameter N_1 on θ and φ fields. It is noted that the fluid temperature positively increases as the radiation parameters vary. Further, Figure 10 shows that the volume fraction boundary layer

thickens near the sheet, while the reverse effect is noticed away from the sheet with the rising values of radiation parameter. Temperature profile decreases with an increase in the magnetic field strength and the concentration field increases with booming magnetic parameter as illustrated in Figures 11, 12. Chemical reactions restrained the thermal and concentration fields (Figures 13, 14). Figure 15 demonstrates typical θ and φ profiles for various values of heat transfer Biot number α_1. An increase in Biot number depicts an increase in the heat transfer coefficient which is responsible for an increase in temperature and thermal boundary layer thickness. Low heat transfer rate is seen for smaller values of heat transfer coefficient, when it gradually increases, the fluid becomes hotter and has a high rate of heat transfer. This concrete behavior can be seen from Figure 16, that its the concentration of nano fluid accumulated due to an increase in the mass transfer Biot number α_2. Thermophoresis parameter increases the temperature and concentration profiles while Brownian motion parameter enhances the temperature profile, while the concentration profile decreases with an increase in Brownian motion parameter as explained in Figures 17, 18. Scrutinizing Table 5, we can see that the heat transfer and mass transfer are enhanced significantly by strengthening the magnetic effect. The same outcomes can be observed by mounting the radiation parameter, heat and mass transfer Biot numbers.

4. Conclusion

Radiative and chemically reactive flow of Eyring Powell nanofluid with non-Fourier's heat flux and non-Fick's mass flux is studied with the consideration of magnetohydrodynamics and convective boundary conditions. The developments of the present paper can be compiled as:

The amplitude of velocity along the abscissa decreases, while the velocity along the ordinate increases with the escalating magnetic effect. Temperature profile increases with the consideration of nanoparticles in the fluid, but the opposite is true for the concentration profile.

Rotational parameter decreases the velocity boundary layer thickness in both directions.

The Eyring Powell fluid parameter has the property of reducing the Nusselt number in both directions.

Author Contributions: Conceptualization, H.F.; Data Collection, H.F. and H.A.; Formal analysis, H.F. and S.M.H.; Investigation, H.A.; Methodology, H.F.; Software, S.T.S. and H.F.; Writing-original draft, H.F. and S.M.H.; Review, S.T.S.; Funding, H.A.; Writing-review and editing, H.A. and S.T.S. All authors have read and agreed to the published version of the manuscript.

Funding: This research received no external funding.

Data Availability Statement: All the data available in this manuscript.

Institutional Review Board: Not applicable

Informed Consent Statement: Not applicable

Conflicts of Interest: The authors declare no conflict of interest.

References

1. Fourier, J. B. J. Théorie Analytique De La Chaleur. Paris **1822**.
2. Cattaneo, C. Sulla conduzione del calore. Atti Semin Mat Fis Univ Modena Reggio Emilia. **1948**, 3, 83–101.
3. Christov, C. I. On frame indifferent formulation of the Maxwell-Cattaneo model of finite-speed heat conduction. *Mech. Res Commun.* **2009**, 36, 481–486.
4. Straughan, B. Thermal convection with the Cattaneo-Christov model. *Int. J. Heat Mass Transf.* **2010**, 53, 95–98.
5. Salahuddin, T.; Malik, M.Y.; Hussain, A.; Bilal, S.; Awais, M. Mhd flow of Cattanneo–Christov heat flux model for williamson fluid over a stretching sheet with variable thickness:using numerical approach. *J. Magn. Magn. Mater*. **2016**, 401, 991–997.
6. Hayat, T.; Nadeem, S. Flow of 3D Eyring-Powell fluid by utilizing Cattaneo-Christov heat flux model and chemical processes over an exponentially stretching surface. *Results Phys.* **2018**, 8, 397–403.
7. Hayat, T.; Farooq, M.; Alsaedi, A.; Al-Solamy, F. Impact of Cattaneo-Christov heat flux in the flow over a stretching sheet with variable thickness. *AIP Adv.* **2015**, 5, 087159.
8. Hashim; Khan, M. On Cattaneo-Christov heat flux model for Carreau fluid flow over a slendering sheet. *Results Phys*. **2017**, 7, 310–319.
9. Abbasi, F. M.; Shehzad, S. A.; Hayat, T.; Alsaedi, A.; Hegazy, A. Influence of Cattaneo-Christov heat flux in flow of an Oldroyd-B fluid with variable thermal conductivity. *Int. J. Numer Methods Heat Fluid Flow*. **2016**, 26, 2271–2282.
10. Hayat, T.; Muhammad, T.; Alsaedi, A.; Mustafa, M. A comparative study for flow of viscoelastic fluids with Cattaneo-Christov heat flux. *PLoS ONE* **2016**, 11, e0155185.
11. Upadhya, S. M.; Raju, C. S. K.; Mahesha; Saleem, S. Nonlinear unsteady convection on micro and nanofluids with Cattaneo-Christov heat flux. *Results Phys*. **2017**, 9, 779–786.
12. Powell, R. E.; Eyring, H. Mechanism for the Relaxation Theory of Viscosity. *Nature* **1944**, 154, 427–428.
13. Hayat, T.; Iqbal, Z.; Qasim, M.; Obaidat, S. Steady flow of an Eyring Powell fluid over a moving surface with convective boundary conditions. *Int. J. Heat MassTransf.* **2012**, 55, 1817–1822.
14. Akbar, N. S.; Nadeem, S. Characteristics of heating scheme and mass transfer on the peristaltic flow for an Eyring–Powell fluid in an endoscope. *Int. J. Heat MassTransf.* **2012**, 55, 375–383.
15. Jalil, M.; Asghar, S. Flow and heat transfer of Powell–Eyring Fluid over a stretching surface: A Lie Group Analysis. *J. Fluids Eng.* **2013**, 135, 121201.
16. Malik, M. Y.; Hussain, A.; Nadeem, S. Boundary layer flow of an Eyring-Powell model fluid due to a stretching cylinder with variable viscosity. *Scientia Iranica* **2013**, 20, 313–321.
17. Nadeem, S.; Saleem, S. Mixed convection flow of Eyring–Powell fluid along a rotating cone. *Results Phys.* **2014**, 4, 54–62.
18. Riaz, A.; Ellahi, R.; Sait, M. S. Role of hybrid nanoparticles in thermal performance of peristaltic flow of Eyring-Powell fluid model. *J. Therm. Anal. Calorim.* 2020, https://doi.org/10.1007/s10973-020-09872-9
19. Hayat, T.; Makhdoom, S.; Awais, M.; Saleem, S.; Rashidi, M. M. Axisymmetric Powell-Eyring fluid flow with convective boundary condition: Optimal analysis. *Appl. Math Mech.* **2016**, 37, 919–928.
20. Ibrahim, W. Three dimensional rotating flow of Powell-Eyring nanofluid with non-Fourier's heat flux and non-Fick's mass flux theory. *Results Phys.* **2018**, 8, 569–577.

21. Makinde, O. D.; Khan, Z. H.; Ahmad, R.; Haq, R. U.; Khan, W. U. Unsteady MHD flow in a porous channel with thermal radiation and heat source/ sink. *Int. J. Appl. Comput. Math* **2019**, 5, 1-21.
22. Nadeem, S.; Akhtar, S.; Abbas, N. Heat transfer of Maxwell base fluid flow of nanomaterial with MHD over a vertical moving surface. *Alex. Eng. J.* **2020**, 59, 1847–1856.
23. Ellahi, R.; Shivanian, E.; Abbasbandy, S.; Hayat, T. Numerical study of magnetohydrodynamics generalized Couette flow of Eyring-Powell fluid with heat transfer and slip condition. *Int. J. Numer. Methods Heat Fluid Flow* **2016**, 26, 1433–1445.
24. Qasim, M.; Hayat, T.; Obaidat, S. Radiation effect on the mixed convection flow of a viscoelastic fluid along an inclined stretching sheet. *Z. Naturforsch* **2012**, 67a, 195–202.
25. Ayub, M.; Khan, T. A.; Jilani, K. Effect of cold plasma permittivity on the radiation of the dominant TEM-wave by an impedance loaded parallel-plate waveguide radiator. *Math. Methods App. Sci.* **2016**, 39, 134–143.
26. Raju, C. S. K.; Saleem, S.; Upadhya, M.; Iqtadar, M. Heat and mass transport phenomena of radiated slender body of three revolutions with saturated porous: Buongiorno's model. *Int. J. Therm. Sci.* **2018**, 132, 309–315.
27. Buongiorno, J. Convective transport in nanofluids. *ASME J. Heat Transf.* **2005**,128, 240–250.
28. Kuznetsov, A. V.; Nield, D. A. Natural convective boundary-layer flow of a nanofluid past a vertical plate. *Int. J. Therm. Sci.* **2010**, 49, 243–247.
29. Khan, W. A.; Pop, I. Boundary-layer flow of a nanofluid past a stretching sheet. *Int. J. Heat Mass Transf.* **2010,** 53, 2477–2483.
30. Nadeem, S.; Haq, R.; Khan, Z. H. Numerical solution of non-newtonian nanofluid flow over a stretching sheet. *Appl. Nano Sci.* **2014**, 4, 625–631.
31. Ahmed, Z.; Nadeem, S.; Saleem, S.; Ellahi, R. Numerical study of unsteady flow and heat transfer CNT-based MHD nanofluid with variable viscosity over a permeable shrinking surface. *Int. J. Numer. Method H.* **2019**, 29, 4607–4623.
32. Alvi, N.; Latif, T.; Qamar, H.; Asghar, S. Peristalsis of nanofluid with temperature dependent viscosity. *J. Comp. Theor. Nano Sci.* **2017**, 14, 1417–1430.
33. Liao, S. J. An optimal homotopy-analysis approach for strongly nonlinear differential equations. *Commun. Nonlin. Sci. Num. Sim.* **2010**, 15, 2003–2016.
34. Nadeem, S.; Mehmood, R.; Akbar, N. S. Optimized analytical solution for oblique flow of a Casson-nano fluid with convective boundary conditions. *Int. J. Therm. Sci.* **2014**, 78, 90–100.
35. Saleem, S.; Firdous, H.; Nadeem, S.; Khan, A.U. Convective heat and mass transfer in magneto Walter's B Nanofluid flow induced by a rotating cone. *Arab. J. Sci. Eng.1* **2019**, 44, 1515–1523.
36. Saleem, S.; Awais, M.; Nadeem, S.; Mustafa, T.; Sandeep, S. Theoretical analysis of upper-convected Maxwell fluid flow with Cattaneo-Christov heat flux model. *Chin. J. Phys.* **2017**, 55, 1615–1625.
37. Awais, M.; Saleem, S.; Hayat, T.; Irum, S. Hydromagnetic couple-stress nanofluid flow over a moving convective wall: OHAM analysis. *Acta Astronautica* **2016**, 129, 271–276.